

Fast gap-filling of massive data by local-equilibrium conditional simulations on GPU

M. Lach · M. Žukovič

Received: date / Accepted: date

Abstract The ever-growing size of modern space-time data sets, such as those collected by remote sensing, requires new techniques for their efficient and automated processing, including gap-filling of missing values. CUDA-based parallelization on GPU has become a popular way to dramatically increase computational efficiency of various approaches. Recently, we have proposed a computationally efficient and competitive, yet simple spatial prediction approach inspired from statistical physics models, called modified planar rotator (**MPR**) method. Its GPU implementation allowed additional impressive computational acceleration exceeding two orders of magnitude in comparison with CPU calculations. In the current study we propose a rather general approach to modelling spatial heterogeneity in GPU-implemented spatial prediction methods for two-dimensional gridded data by introducing spatial variability to model parameters. Predictions of unknown values are obtained from non-equilibrium conditional simulations, assuming “local” equilibrium conditions. We demonstrate that the proposed method leads to significant improvements in both prediction performance and computational efficiency.

Keywords spatial interpolation · local-equilibrium simulation · non-Gaussian model · heterogeneous data · GPU parallel computing · CUDA

1 Introduction

With the emergence and increasing frequency of massive spatio-temporal data sets, such as those collected by remote sensing technologies, scalable numerical techniques are required for their efficient processing. For example, such data often include gaps that may occur as a result of sensor malfunctions, cloud, vegetation or snow coverage, dense precipitation or other barriers separating the sensed object and the remote sensing device (Lehman et al., 2004; Coleman et al., 2011; Bechle et al., 2013; Sun et al., 2017; Kadlec and Ames, 2017) and may have the unfavorable effect on

Department of Theoretical Physics and Astrophysics, Institute of Physics, Faculty of Science, Pavol Jozef Šafárik University in Košice
Park Angelinum 9, 041 54 Košice
Tel.: +421-55-2342544
E-mail: milan.zukovic@upjs.sk

statistical assessment of mean values and trends. Therefore, they need to be estimated to generate gapless maps of observed variables and to facilitate prompt and informed decisions (Sickles and Shadwick, 2007). Most of traditional interpolation methods, such as kriging (Wackernagel, 2003), however, are not directly applicable to such massive data due to their computational demands. Consequently, several modifications of kriging-based methods have been developed (Furrer et al., 2006; Cressie and Johannesson, 2018; Hartman and Hössjer, 2008; Kaufman et al., 2008; Ingram et al., 2008; Zhong et al., 2016; Oyebamiji et al., 2017; Marcotte and Allard, 2018), in effort to increase their computational efficiency.

Very recently, a geostatistics-informed machine learning model has been suggested by Bai and Tahmasebi (2021) to improve the computational performance of the ordinary kriging and inverse distance weighted regression method Emmendorfer and Dimuro (2021) to improve the performance of the standard inverse distance weighted (IDW) method (Shepard, 1968). Aiming at the same goal, a statistical physics inspired approach that employs models based on Boltzmann-Gibbs exponential joint densities has also been proposed (Hristopulos, 2003; Hristopulos and Elogne, 2007; Hristopulos, 2015; Žukovič and Hristopulos, 2009a,b; Žukovič and Hristopulos, 2018; Hristopulos et al., 2021). In this concept, spatial correlations are captured by means of short-range interactions, instead of the experimental variogram used in geostatistical methods, which renders the proposed interpolation methods computationally very efficient. Especially, the recently introduced method that employed the *modified planar rotator* (MPR) model (Žukovič and Hristopulos, 2018), due to its computational efficiency (roughly linear-time computation complexity) and ability to operate autonomously without user input, was shown to be appropriate for the automated and efficient processing of massive gridded data, typical in remote sensing.

Nevertheless, spatial simulation performed in a sequential way is still computationally costly, especially in the case of simulating huge data sets (Mariethoz, 2010; Nunes and Almeida, 2010; Peredo et al., 2015; Rasera et al., 2015). With new developments in hardware architecture and its availability in common PCs, in particular multi-core CPU and general purpose Graphics Processing Units (GPU), more and more popular way of overcoming the computational inefficiency is achieved by parallel implementations. Up to date most standard interpolation methods, including kriging and IDW, have been parallelized on high performance and distributed architectures (Kerry and Hawick, 1998; Cheng et al., 2010; Guan et al., 2011; Pesquer et al., 2011; Hu and Shu, 2015; Misra et al., 2020; Que et al., 2021; Migallón et al., 2022) and general-purpose computing GPU (Xia et al., 2011; Tahmasebi et al., 2012; Cheng, 2013; de Ravé et al., 2014; Mei, 2014; Stojanovic and Stojanovic, 2014; Mei et al., 2017; Marcellino et al., 2017; Zhang et al., 2019, 2018). It has been shown that by means of parallelization, it is possible to achieve computational acceleration achieving up to almost two orders of magnitude compared to traditional single CPU implementation.

Parallelization of spin models simulation is achievable due to the short-range character of interactions between the spin variables. By employing a highly parallel architecture of GPUs impressive up to 1000-fold speedups can be achieved (Weigel, 2011, 2012). Our recent GPU implementation of the spin-model-based MPR method led to almost 500-fold computational speedup, compared to single-processor calculations, for massive data sets (Žukovič et al., 2020). Thus, using an ordinary personal computer, data sets that involve even several millions of points can be processed in a fraction of second.

Most of geostatistical methods assume spatial homogeneity/stationarity of data, even though recently a kriging-based interpolation method for non-homogeneous data has been proposed (Lajounie et al., 2020). However, if one targets large spatial data, in which anisotropy and non-stationarity are common, such an assumption is not justified. It is not reasonable to assume that one set of

model parameters can capture scale-dependent relationships between covariates and the outcome variable that vary in space. The most common techniques for modelling such data are geographically weighted regression (GWR) and spatially-varying coefficients (SVC) methods (Fotheringham et al., 2003; Gelfand et al., 2003; Harris et al., 2010a; Finley, 2011). There are some relatively efficient GWR methods that have been developed (Harris et al., 2010b; Tran et al., 2016; Li et al., 2019) but the scalable linear-time implementation required for application to big data sets has been proposed only very recently (Murakami et al., 2020). Their parallelization via the Message Passing Interface lead to a further increase in computational efficiency (Li et al., 2019). Another recent approach to modeling large data with non-stationary covariance structure is based on efficient local likelihood estimation in moving windows to infer spatially varying covariance parameters (Pardo-Igúzquiza et al., 2005; Wiens et al., 2020).

In the present paper we implement modifications to our previously introduced GPU-accelerated **MPR** method in effort to enable modeling spatial heterogeneity/non-stationarity, essential for analyzing massive spatial data. In the GPU-implemented version this can be conveniently achieved by introducing spatial dependence to the **MPR** model parameter (temperature) by the so-called double checkerboard decomposition. Then, predictions of unknown values are obtained from non-equilibrium conditional situations, assuming “local” equilibrium conditions corresponding to local temperatures varying in space (MacGillivray et al., 1993).

The rest of the paper is structured as follows: in Section 2 we present an overview of the previously introduced **MPR** model and its GPU implementations with both spatially-uniform and spatially-varying parameters; more details are given in Žukovič and Hristopulos (2018) and Žukovič et al. (2020). The statistical and computational performance of the **MPR**-based models is investigated and compared to the standard approach in Section 3. In the last Section 4 we summarize our findings and present conclusions.

2 **MPR** methods

2.1 **MPR** method with spatially uniform parameter

Let us consider a two-dimensional square grid \mathcal{G} of the size $L \times L$ nodes with partially known values (samples). Let us denote locations of the samples of the spatial process $Z(\mathbf{s})$ on the grid nodes as $\mathcal{G}_S = \{\mathbf{s}_n\}_{n=1}^N$, where $N < L^2$ and their values as $\mathbf{Z}_s = (z_1, \dots, z_N)^\top$ (where \top denotes the matrix transpose). The task is to estimate the missing values $\hat{\mathbf{Z}}_p = (\hat{z}_1, \dots, \hat{z}_P)^\top$ of the process at the grid nodes $\mathcal{G}_P = \{\tilde{\mathbf{s}}_p\}_{p=1}^P$. Thus, the intersection of the sets \mathcal{G}_P and \mathcal{G}_S is empty and their union represents the full grid \mathcal{G} .

In the following we briefly outline the basic idea of the **MPR** method, recently introduced for efficient and automatic prediction of partially sampled non-Gaussian data on regular grids (Žukovič and Hristopulos, 2018). It should be noted that, unlike geostatistical methods, the **MPR** method makes no restrictive assumptions regarding the probability distribution of the spatial process. Instead, it assumes that the spatial correlations are imposed by local (nearest-neighbor) interactions between the nodes of \mathcal{G} . The **MPR** method employs the modified planar rotator (**MPR**) spin model in the framework of a Gibbs-Markov random field (GMRF). In the first step, the original data are linearly transformed to continuously-valued “spin” variables (or spin angle ϕ) space $[0, 2\pi]$. Then,

conditional Monte Carlo (MC) simulations of the **MPR** Hamiltonian

$$\mathcal{H} = -J \sum_{\langle i,j \rangle} \cos[q(\phi_i - \phi_j)], \quad (1)$$

where $J > 0$ is the interaction between neighboring spins and $q \leq 1/2$ is the modification parameter, are performed at the temperature T . The latter is estimated by matching of the specific energy of the whole grid (including sample and prediction points) with that calculated only from samples as

$$e_s = -\frac{1}{N_{SP}} \sum_{i=1}^N \sum_{j \in nn(i)} \cos[q(\phi_i - \phi_j)], \quad (2)$$

where $j \in nn(i)$ is the sum over the sample (non-missing) nearest neighbors of the site \mathbf{s}_i (i.e., $\mathbf{s}_j \in \mathcal{G}_S$), and N_{SP} is the total number of the nearest-neighbor sample pairs. After reaching thermodynamic equilibrium, the spin values at the prediction locations are back-transformed to the original values. Finally, spatial prediction of missing data is based on taking the mean of the respective conditional distribution at the target site given the incomplete measurements. Its high computational efficiency makes the **MPR** method applicable to massive data, for example remotely sensed images. More details about the **MPR** algorithm can be found in the paper by [Žuković and Hristopulos \(2018\)](#).

2.2 **SV-MPR** method with spatially varying parameter

While the **MPR** model has proved to be competitive for non-Gaussian data, its reliance on the single parameter - the reduced temperature T - for the whole data set naturally restricts its applicability. In particular, since T is related to spatial variability, a single parameter value cannot adequately capture spatial variability of the data showing some heterogeneity, a commonly present feature in massive data. For example, if the studied data set includes domains of almost constant values as well as domains with large spatial fluctuations, no single value of T can be optimal for both of these regimes. The sample specific energy given by Eq. (2) in a subsystem with nearly constant values will be very low, which will result in T taking values close to 0. Such values would not be representative for a subsystem with high variability and vice-versa. The sample specific energy calculated from all data (including domains with low and high variability) and subsequently estimated temperature thus may not be characteristic for either of the involved domains. As a result, the spatial variability of the predictions in the domains with low (high) variability will be over- (under)-estimated.

2.2.1 GPU-implemented **SV-MPR** method

Generally, such a problem can be addressed by introducing a spatial dependence into the model parameters, as it is done in the GWR approach ([Fotheringham et al., 2003](#); [Gelfand et al., 2003](#)). The current implementation in CUDA offers a very straightforward way to do this for the **MPR** method. Parallel computations in CUDA are facilitated by virtual processors called threads that can be mapped to hardware resources to perform computations for individual (or multiple) data points or spins. These threads are organized into blocks consisting of up to 1024 threads arranged in one, two or three dimensions (here, we use square blocks). Thread blocks are in turn organized

into a grid of up to three dimensions. Block and grid dimensions are specified at the launch of each kernel - a function which executes computations on the GPU. More information about the CUDA programming model and the implementation of the MPR algorithm on the GPU is given in our previous paper (Žukovič et al., 2020).

2.2.2 Block-specific parameter inference and simulation

The energy of the system is calculated using the parallel reduction algorithm (Harris, 2007; Luitjens, 2014). Each thread is mapped to a single spin and computes the energy of a bond with two of its neighbors using the Hamiltonian (1) in such a way that all the bonds present in the system are counted. Then, the results of each thread within a given block are *reduced* (summed) to a single value representing the energy contribution of that block. Since at this point, the energy is known for each block, same energy matching procedure as described in Sect. 2.1 can be used to assign an individual value of T to each block. Thus, we obtain multiple values of the simulation parameter T for different regions of the system. In the extreme case, when a large percentage of the block's data is missing and there are no bonds between samples (no nearest neighbors) for energy calculation and temperature estimation, such a block will be assigned the temperature corresponding to the median value of the available block temperatures.

Since during simulation, threads representing individual spins are also grouped into blocks, instead of a single global value of T , each thread can use the value which corresponds to the block it belongs to. One must make sure that the same configuration of thread blocks used for the energy computation is also used for the Metropolis update, otherwise spins from one part of a system may end up using a temperature based on a different part of the system with diverse behavior. This approach synergizes with an optimization technique called double checkerboard (DC) decomposition (Weigel, 2012), which is an extension of the single checkerboard (SC) decomposition described in our previous paper (Žukovič et al., 2020).

Assuming the data are localized on a two dimensional square grid (generalization to any regular grid is straightforward), they can be split into two sets sitting on two interpenetrating sub-grids, e.g., A and B. The nearest neighbors of any node on the sub-grid A belong to the sub-grid B, and vice versa. Therefore, the updating algorithm can be applied to all the spins on the same sub-grid in parallel. In Fig. 1, the two sub-grids are depicted using light and dark *small* squares. Our computation kernels call one thread per each sub-grid spin.

The DC decomposition splits the grid further into larger tiles, which correspond to thread blocks. At each MC step, first only the even (odd) numbered tiles are updated in parallel and then only the odd (even) tiles. Each tile can be loaded into the block's shared memory, which is orders of magnitude faster compared to the GPU's global memory, and we can perform multiple Metropolis updates in quick succession only within the even numbered blocks, before doing the same for the odd numbered blocks. As mentioned above, since the temperature is computed individually for each block, we can assign a different value to each tile of the decomposed grid, as depicted in Fig. 1 using light and dark *large* squares. In our case, this is the main reason for using the DC decomposition as we do not apply the update procedure multiple times for individual tiles. Nevertheless, due to the fact that the tiles are first loaded into shared memory, looking up the neighboring spins uses shared instead of global memory and we still get a small performance benefit, as will be discussed below. More information about the various types of memory available on GPUs can be found in our previous paper (Žukovič et al., 2020) and in the CUDA programming manual (Nvidia, 2021).

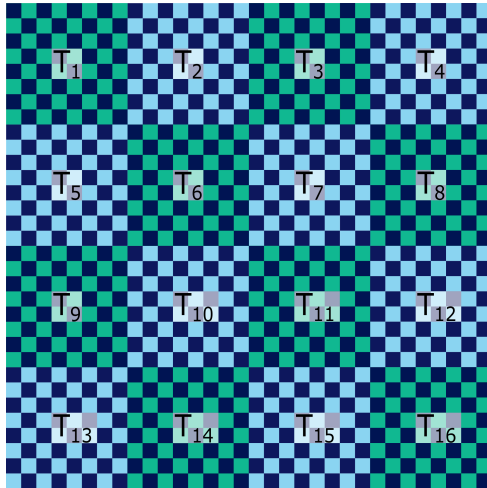


Fig. 1 Schematic representation of a double checkerboard decomposition of the spin grid with block specific temperatures T_i , $i = 1, \dots, 16$. Each small square represents a grid node with its associated spin variable. Each thread performs calculations for a single spin. Sub-grid A comprises the dark nodes, while sub-grid B includes the light nodes. The grid is decomposed further into larger dark and light tiles corresponding to individual thread blocks responsible for the numerical operations on the spins included within the tile. Each tile can be simulated using a different temperature computed only from the spins within the tile.

We call this version of the algorithm using the DC decomposition as the **SV-MPR** method with block-specific temperatures (BST).

2.2.3 Site-specific parameter inference and simulation

Our second approach is motivated by the effort to eliminate the undesirable block boundary effect that occurs in the above **SV-MPR** method with BST. It results from the fact the temperature varies on the grid discontinuously as a step function and thus neighboring blocks assigned markedly different temperature values will be characterized with markedly different spatial variations of the simulated values, which can generate unnatural edges between blocks on the prediction map. Such an effect can be partially reduced by decreasing the size of the blocks. However, this approach has some limitations as very small blocks may lack samples either completely or their reduced numbers within blocks may lead to imprecise block-specific temperature estimation. An alternative approach allows us to reduce the block size so that each of them contains only one spin and thus to obtain a smooth variation of temperatures on the grid. Assigning a value of T to each spin individually can be viewed as a limiting case of decreasing the block size $l_b \rightarrow 1$. However, instead of actually decreasing the block size we apply a simple smoothing algorithm to the block temperatures. The latter can be achieved by starting from the BST state and recursively replacing the temperature at each site with an average value of the surrounding area with some radius r_s . To reach the desired level of smoothness, it can be applied n_s times in succession. We will refer to this version of the algorithm as the **SV-MPR** method with site-specific temperatures (SST). The implementation of the **SV-MPR** algorithms on the GPU is illustrated in the flowchart shown in Fig. 2.

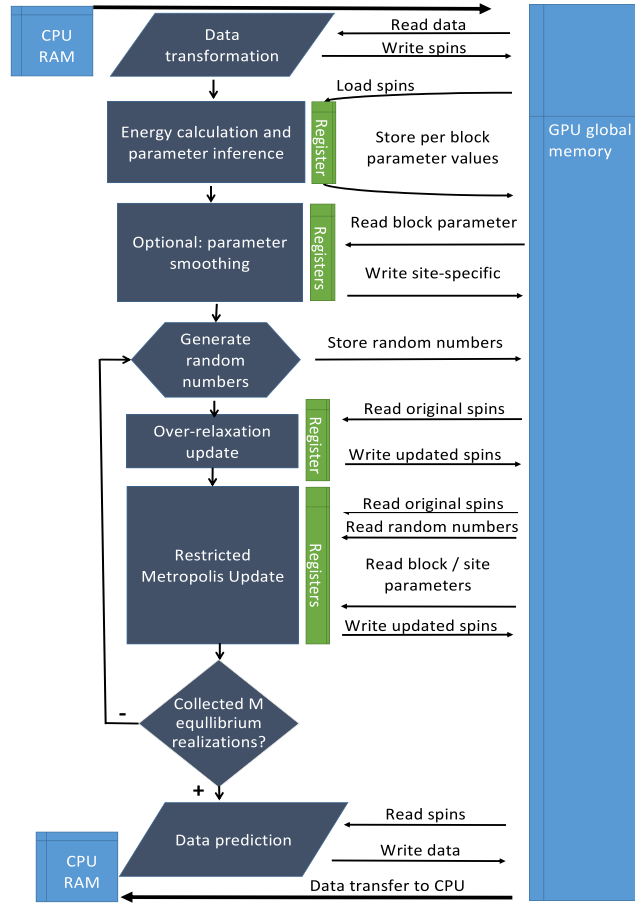


Fig. 2 Flowchart of the main computational steps and memory transactions performed on the GPU.

3 Results

3.1 Data

To assess the effect of introducing the spatial dependence into the model parameter, we compare both the prediction performance and computational efficiency of the present **SV-MPR** model with the original **MPR** model. The comparison is performed on several big real world data sets showing a heterogeneous character of their spatial variability (see Fig. 3) and non-Gaussian (skewed, multimodal, etc.) distributions (see Fig. 4). The first one represents the synthetic pollutant concentration data derived from a digital elevation model of the Walker lake area in Nevada (Isaaks and Srivastava, 1989). A map showing a 2D projection of the pollution field is presented in Fig. 3(a) along with the histogram on a semi-log scale in Fig. 4(a). The units used for the Z values are arbitrarily set to parts per million (ppm). The map shows the presence of both larger dark regions with the values close to zero and almost no variability, as well as brighter regions with very large

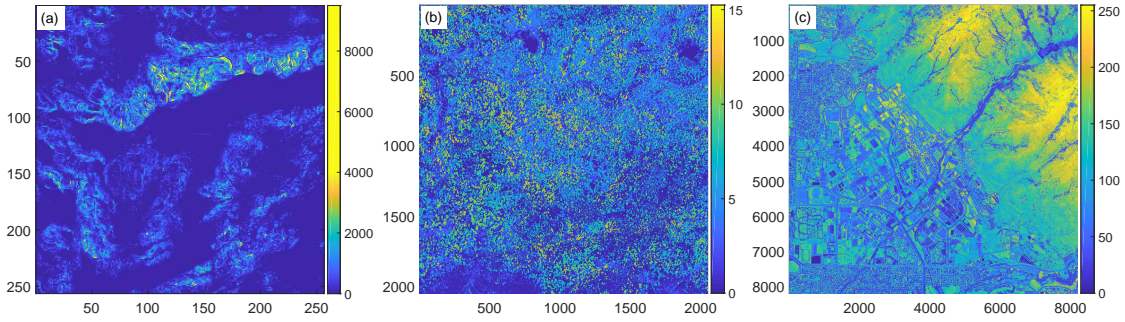


Fig. 3 Spatial distributions of (a) Walker lake, (b) Kaibab plateau and (c) Wasatch front.

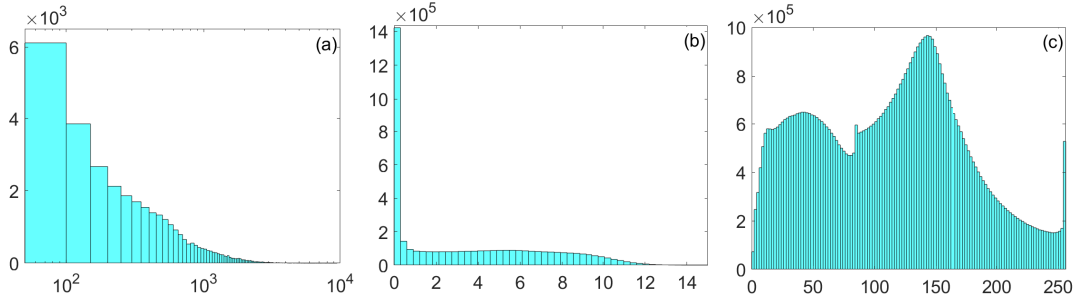


Fig. 4 Histograms of (a) Walker lake, (b) Kaibab plateau and (c) Wasatch front.

values and relatively high variability¹. The histogram shows that the distribution is highly positively skewed indicating the predominance of very low concentrations with just a small portion of extremely large values.

Further, we considered much larger data sets with the linear grid sizes $L = 2\,048$ and $L = 8\,192$, collected using airborne light detection and ranging (LIDAR) technology. They represent the canopy height (in meters) of the forests around Kaibab plateau, Arizona (US Forest Service, 2019) (Figs. 3(b) and 4(b)), and the digital surface model of Wasatch front, Utah (State of Utah, 2015) (Figs. 3(c) and 4(c)). These data sets include values over extensive spatial domains with nontrivial distributions, as shown in the histograms in Fig. 4. The statistical properties of all the data sets are summarized in Table 1.

Table 1 Summary statistics of the used data sets.

Dataset	Number of points	Range	\bar{z}	$z_{0.50}$	σ_z	skewness	kurtosis
Walker lake	65 535 ($L = 256$)	0 – 9 500	289	64	516	3.6	23.3
Kaibab plateau	4 194 304 ($L = 2\,048$)	0 – 15	3.6	2.7	3.5	0.58	2
Wasatch front	67 108 864 ($L = 8\,192$)	0 – 255	112	117	62	0.13	2.2

¹ Note the adjusted color map, showing all the values $Z \gtrsim 4\,000$ in yellow, to better visualize the extreme data in the tail.

3.2 Prediction validation

To evaluate the performance of the **MPR**-based prediction algorithms, we simulate missing values by setting aside a portion of the complete data to be used as a validation set. We typically generate $M = 100$ different configurations by randomly removing between $p = 30\% - 90\%$ (or $p = 0.3 - 0.9$) of data points. The **MPR** predictions are based on the conditional mean as evaluated from the conditional MC simulation. The reconstructions are compared with the true values, first by visually inspecting the reconstructed data and then statistically, using two validation measures: the average absolute error (AAE) defined as

$$\text{AAE} = \frac{1}{P} \sum_{\mathbf{r}_p \in G_p} |\epsilon(\mathbf{r}_p)|, \quad (3)$$

and the root average squared error (RASE)

$$\text{RASE} = \sqrt{\frac{1}{P} \sum_{\mathbf{r}_p \in G_p} \epsilon^2(\mathbf{r}_p)}, \quad (4)$$

where $\epsilon(\mathbf{r}_p) = Z(\mathbf{r}_p) - \hat{Z}(\mathbf{r}_p)$ is the difference between the true value $Z(\mathbf{r}_p)$ and the predicted value $\hat{Z}(\mathbf{r}_p)$ at the site \mathbf{r}_p and $P = pL^2$ is the number of prediction sites. Both of these quantities are then averaged over the $M = 100$ different sample configurations to calculate the mean AAE (MAAE) and mean RASE (MRASE). CUDA-based calculations are executed on a PC with NVIDIA GeForce RTX 2080 SUPER GPU, using CUDA version 10. The CPU host system is equipped with 8-core 3 GHz Intel(R) Core(TM) i7-9700F CPU with 32 GB RAM, running Ubuntu 20.04.3 LTS Linux.

3.3 Visual inspection of reconstructions

3.3.1 Standard **MPR** method

Let us first demonstrate the performance of the original **MPR** algorithm with a single (spatially uniform) parameter T and its weak point, especially when applied to the data with highly heterogeneous spatial variability, such as the Walker lake data set. The gappy data along with their reconstructions using the **MPR** algorithm are depicted in Fig. 5 for three values of the thinning ratio $p = 30\%, 60\%$ and 85% . The **MPR** algorithm performs fairly well for small values of p , thanks to the abundance of the conditioning sample data. However, with the increasing sparsity of the samples the prediction performance quickly deteriorates. In particular, the predicted values in the regions corresponding to very low or zero concentrations (dark regions) noticeably overestimate the true values, which is reflected in the appearance of speckles with lighter colors. On the other hand, the extremely large values are greatly underestimated, albeit it is less conspicuous in the reconstructed map due to the scarcity of such data. This phenomenon becomes much more pronounced at larger concentrations of missing data (lack of conditioning sample data), such as for $p = 85\%$ presented in Fig. 5(f). This problem is not conspicuous on the large scale but it is evident if we zoom in a small area, as shown in the inset. In this particular area the true values are $Z(\mathbf{r}_p) = 0$, nevertheless, the predictions $\hat{Z}(\mathbf{r}_p) \in [0, 100]$. Considering the fact that the **MPR** model includes only one parameter, this averaging effect is not surprising. The temperature \hat{T} is estimated based on all the samples, involving regions with different degrees of spatial variability

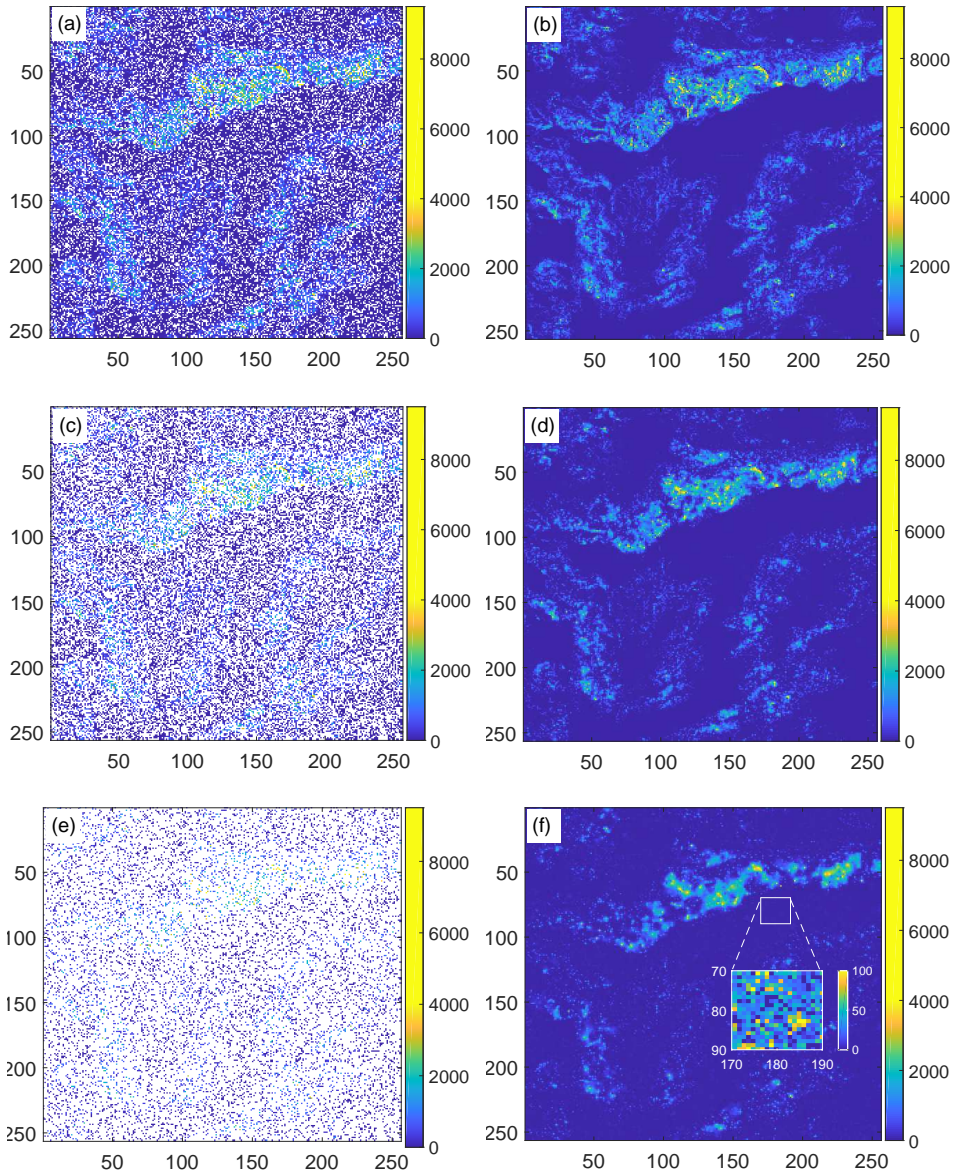


Fig. 5 Original Walker lake data with (a) $p = 30\%$, (c) $p = 60\%$ and (e) $p = 85\%$ of the data (white color) randomly removed and the corresponding MPR-based reconstructions obtained at the (spatially uniform) temperatures (b) $\hat{T} = 0.0378$, (d) $\hat{T} = 0.0378$ and (f) $\hat{T} = 0.0672$, respectively.

and, thus the resulting mean value of \hat{T} cannot be representative in all these areas and thus cannot reflect the local conditions.

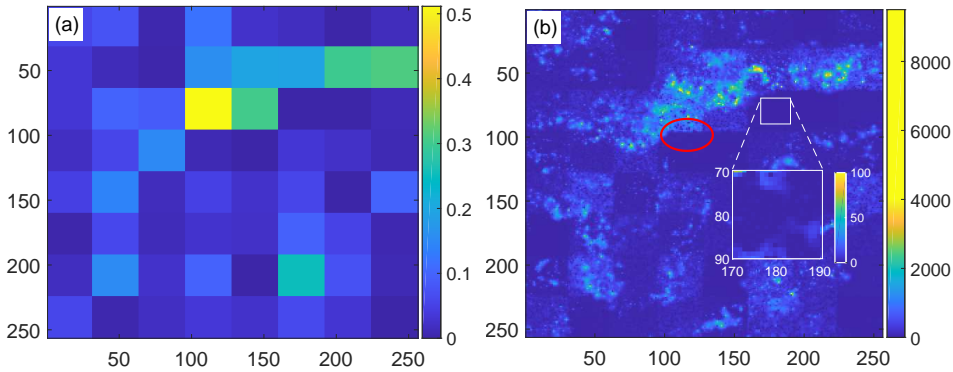


Fig. 6 (a) Distribution of block-specific temperatures and (b) map of reconstructed data using the BST implementation of the **SV-MPR** method for $l_b = 32$. The red ellipse encloses an example of the edge-like artifact of using block-specific temperatures and the square area demonstrates the improved **SV-MPR** predictions compared to the **MPR** ones in the same area shown in Fig. 5(f).

3.3.2 **SV-MPR** method - BST implementation

To best demonstrate the beneficial effects of implementing spatial variability of the parameter in the presently introduced **SV-MPR** versions of the algorithm, we chose the high sample sparsity case of $p = 0.85$ (85%). The **MPR** reconstruction is depicted in Fig. 5(f) and the corresponding (spatially uniform) parameter value, estimated from the specific energy matching principle based on all samples, is $\hat{T} = 0.0672$. By using the double checkerboard decomposition in the **SV-MPR** implementation the spatial distribution of the estimated block-specific temperatures (BST) with square blocks of the linear size $l_b = 32$ is shown in Fig. 6(a). One can witness a great variability in BST, the values of which correlate with the sample variation in the respective blocks. In particular, the blocks with almost constant sample values close to zero are assigned very low values of $\hat{T} \approx 0$, while those with spatially highly variable samples are assigned much higher values of up to $\hat{T} \approx 0.5$. It is worth noticing that the mean value of $\hat{T} = 0.0693$, calculated over all blocks, coincides rather well with the **MPR** estimate \hat{T} . Consequently, one can expect that the spatially-variable parameter can better model the local data variability than the spatially-uniform one. Indeed, performing simulations using the **SV-MPR** (BST) implementation with the block specific temperatures yields the reconstruction, which suffers much less from the averaging effect than the **MPR** method, as demonstrated in Fig. 6(b). Visually, the reconstruction is much closer to the original data than that of the original **MPR** algorithm, especially in the (dark) regions with low spatial variability. For comparison, the inset shows the **SV-MPR** predictions in the same area as for the **MPR** method in the inset of Fig. 5(f), for which $\hat{Z}(\mathbf{r}_p) \in [0, 20]$. On the other hand, undesirable artifacts resulting from the presence of boundaries between blocks with different parameters appear (see, e.g., the area marked by the red ellipse in Fig. 6(b)). Such unnatural edge-like effects are likely to emerge between blocks which include sample data with distinct degrees of variability. We note that the edges are partially smeared due to the fact that the spins at the shared boundaries of the neighboring blocks interact with each other and thus propagate fluctuations from their blocks to the surrounding blocks. Nevertheless, such a diffusion has a local character with rather limited range and cannot eliminate the edge-like effects completely. To further eliminate these undesirable artifacts, we tried

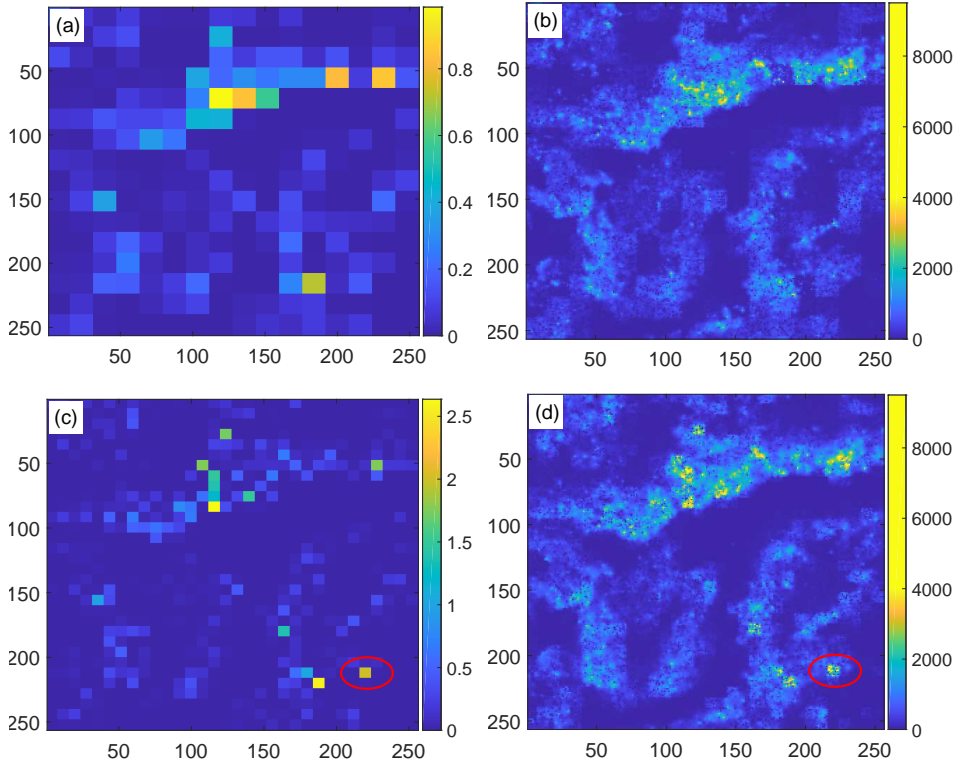


Fig. 7 Distributions of block-specific temperatures (left column) and the corresponding data reconstructions (right column) using the **SV-MPR** (BST) implementation for $l_b = 16$ (upper row) and $l_b = 8$ (bottom row). The red ellipses in the lower panels highlight the area of misestimated parameter (panel (c)) and consequently data variability (panel (d)) due to lack of samples in the corresponding block.

two approaches. The first one consists in gradually decreasing the linear block size l_b from 32 to 16 and 8. The block temperatures (left column) and the corresponding data reconstructions (right column) are shown in Fig. 7, for $l_b = 16$ (top row) and $l_b = 8$ (bottom row). Decreasing the block size leads to partial elimination of the conspicuous edges between blocks and also allows a greater flexibility in capturing the local variability. On the other hand, the decreasing block size also reduces the amount of the neighboring sample pairs (bonds) available for the calculation of the block-specific sample energies, and thus inhibits a reliable estimation of the block-specific temperatures. Particularly for very sparse samples with high values of p , this may cause insufficient statistics for a reliable estimation of the block-specific temperatures. This leads to the second type of the artifacts in the form of misestimation of the data variability due to the erroneous parameter estimation (see, e.g., the bright square in the lower right corner of Fig. 7(d) showing unexpectedly large variability including extremely large values due to the overestimation of \hat{T}). Notwithstanding, the presented results also demonstrate that decreasing granularity of the blocks results in a smoother spatial variation of the parameter and considerably suppresses the block boundary effects.

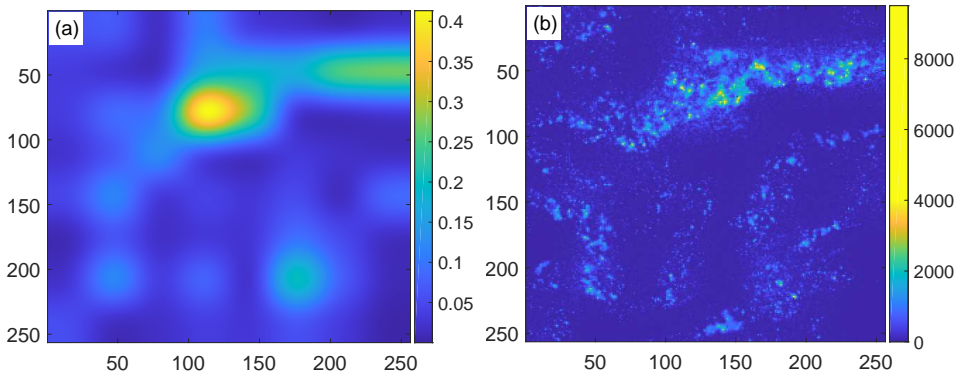


Fig. 8 (a) Temperature map after applying the smoothing algorithm with $n_s = 5$ to block temperatures with $l_b = 32$. (b) Walker Lake data reconstruction for $p = 0.85$ by using the single checkerboard implementation with site-specific temperatures (SST).

3.3.3 *SV-MPR* method - *SST* implementation

The second implementation of the *SV-MPR* model attempts to eliminate the artifacts associated with the BST approach by applying a smoothing algorithm to the block-specific temperatures to obtain a smooth variation of the temperature values over the entire grid. Consequently, each site is assigned an individual value of the reduced temperature and thus this implementation will be referred to as the *SV-MPR* method with site-specific temperatures (SST). The block-specific temperatures for Walker lake data with $l_b = 32$ (see Fig. 6(a)) after smoothing are shown in Fig. 8(a). Using these local temperatures in the conditional simulations we obtain the data reconstruction for the Walker lake data, shown in Fig. 8(b). Notice that the unnatural boundary effects from the BST implementation are now completely eliminated while the spatial variability in different regions is reproduced much better than in the original *MPR* method (compare to Fig. 5(f)). In principle in this *SV-MPR* (SST) implementation both the standard single and the double checkerboard decompositions can be used but for simplicity, we have chosen to use the former one. Applying the *SV-MPR* approach in Fig. 9 we also visually present the results of the reconstruction of the Kaibab plateau and Wasatch front data sets after randomly removing $p = 85\%$ of pixels.

We note that in both the BST and the SST implementations, due to the splitting of the simulations on a large grid into a number of parallel simulations in much smaller blocks (including at most hundreds of sites), the equilibration even faster than in the original *MPR* method. To demonstrate the impact of the domain spitting used in the *SV-MPR* methods, in Fig. 10 we illustrate the equilibration process in the biggest Wasatch front data set with $p = 0.3$. In particular, we show the evolution of the specific energy e , calculated for the whole grid, in the respective *MPR*-based methods averaged over 100 realizations. One can notice that even though a random initialization in the *MPR* method results in the initial value of e far from the equilibrium value, the relaxation process is relatively fast even for such large data set requiring only about 30 MC sweeps. Nevertheless, the *SV-MPR* BST and SST implementations can shorten it even more due to the initialization by the per-block averages, corresponding to the specific energies much closer to equilibrium values. It is also interesting to compare the equilibrium energy values e_{eq} resulting from

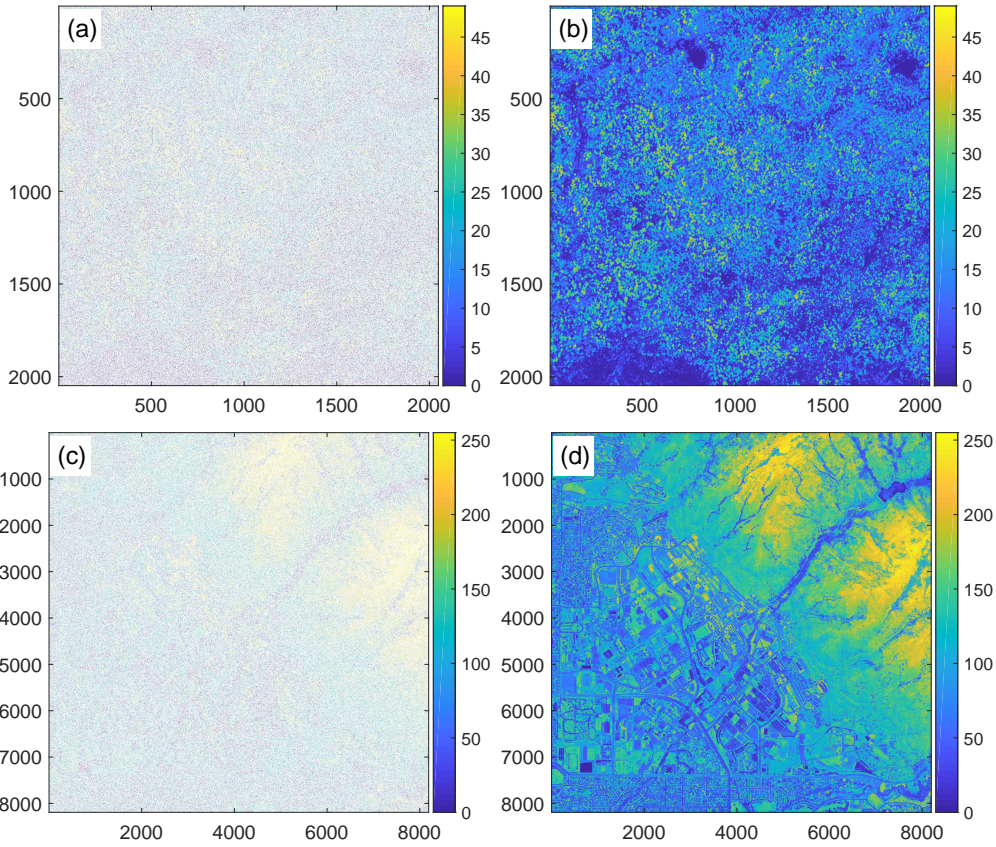


Fig. 9 (a,c) Samples of the Kaibab plateau and Wasatch front, obtained by removing $p = 85\%$ of pixels, and (b,d) their reconstructions obtained by the **SV-MPR** SST method.

different approaches among each other as well as with the sample-estimated value e_s (see Eq. (2)). One can see that while the **MPR** method gives e_{eq} close to e_s , the BST and SST implementations give the values of e_{eq} respectively higher and lower than e_s . The increased BST value can be explained by the presence of boundaries between different blocks, which create unnatural domain walls and thus increase the total energy. On the other hand, the smoothing of the temperatures in the SST implementation leads to partial elimination of the domain walls, not only those unnaturally created by the BST approach but also those substantiated by the data.

3.4 Statistical validation

The results for the Walker lake data set obtained by the standard **MPR** method as well as the **SV-MPR** BST and SST implementations are shown in Table 2 in terms of the prediction errors and computational times for different degrees of the sample sparsity. As expected, both MAAE and MRASE errors increase with higher ratios of the missing data p for all implementations. Nevertheless, it is clear that implementing a spatial dependence in the simulation temperature has a

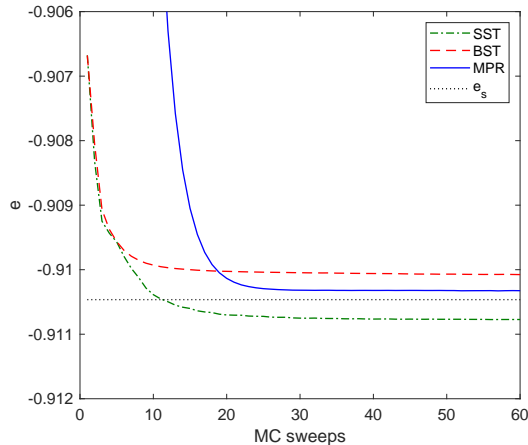


Fig. 10 Evolution of the specific energy during equilibration process in the respective **MPR**-based methods for the Wasatch front data with $p = 0.3$ averaged over 100 realizations. e_s represents the average of the sample energy.

significant positive effect on the prediction accuracy. Compared to the **MPR** approach with a single global temperature the values of both MAAE and MRASE in the **SV-MPR** implementations are considerably smaller for all p . The relative improvements achieved by the present implementations are demonstrated in Fig. 11, in which we present error ratios of the respective methods as a function of the data thinning. Not surprisingly, the benefits of the parameter spatial variability increase with the increase of the sample sparseness, i.e., the decrease of the amount of the local conditioning data. The relative MAE (MRASE) errors decrease up to $p \approx 0.7$ ($p \approx 0.8$), where the **SV-MPR** accuracy outperforms the **MPR** one by up to 11% (15%), and then they start increasing. Their increase for very large p is related with the above discussed artifacts of the second kind - misestimation of the local (block-specific) parameters due to insufficient statistics within the respective blocks. By comparing the BST and SST implementations of the **SV-MPR** approach, the former appears to be more accurate for smaller p , while the benefits of the latter show up more at intermediate and larger p . As already demonstrated by Žukovič et al. (2020), the GPU implementation of the **MPR** model resulted in a computationally very efficient prediction method. In the Walker lake data set the **MPR** prediction of arbitrarily large portion of missing data takes no more than 8 ms, with no apparent dependence on p . Both the BST and SST implementations of the **SV-MPR** algorithm, besides the above demonstrated increasing of the prediction accuracy, also further decrease the computational burden with the computational time squeezed to 5-7 ms. The computational complexity of the **SV-MPR** algorithm will be discussed in a more detail below.

The results for the remaining (much larger) data sets are summarized in Table 3 for the missing data ratio $p = 0.85$. The expected degree of the improvement in the prediction performance, resulting from the introduction of spatial dependence in the parameter, can be judged from the character of the data under consideration. The Walker lake data set with the extensive areas corresponding to (almost) constant values is an example of the spatial distribution which can greatly benefit from the spatially-variable parameters. To certain extent similar features, with some larger areas of constant values, can also be observed in the remaining data sets. Therefore, the **SV-MPR** implementations can also be expected to deliver better prediction performance than

Table 2 Validation measures for the three implementations of the **MPR**-based prediction algorithm for various missing data ratios p applied to the Walker lake pollution data set. All implementations use single precision (FP32) arithmetic with hardware intrinsic CUDA functions, $l_b = 32$ and for the SST implementation $n_s = 5$.

p	MPR			SV-MPR (BST)			SV-MPR (SST)		
	MAAE	MRASE	t[ms]	MAAE	MRASE	t[ms]	MAAE	MRASE	t[ms]
0.1	177	352	7.3	163	331	6.2	167	333	6.4
0.2	180	359	7.5	165	336	6.3	168	336	6.9
0.3	186	367	7.5	168	340	6.5	169	338	6.6
0.4	190	378	7.8	171	347	5.3	172	342	6.3
0.5	196	391	7.6	176	355	5.3	175	348	5.7
0.6	203	405	7.5	181	364	5.2	180	354	5.4
0.7	212	423	7.5	189	376	5.2	188	363	5.3
0.8	221	443	8.0	202	390	5.3	204	378	5.3
0.85	225	451	7.5	217	401	5.3	221	392	5.4

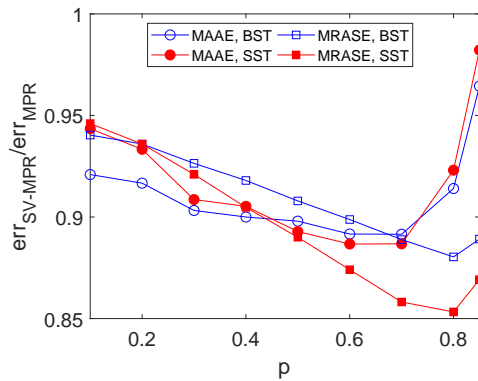


Fig. 11 Errors of the **SV-MPR** implementations (BST and SST), err_{SV-MPR} , relative to those obtained from the simple **MPR** method, err_{MPR} , as functions of the data thinning p , for the Walker lake data set.

Table 3 Validation measures for the three implementations of the **MPR**-based prediction algorithm for the Kaibab plateau and Wasatch from data sets with missing data ratio $p = 0.85$. The implementations use single precision (FP32) arithmetic with hardware intrinsic CUDA functions. The linear sizes of these data sets are: $L = 2\,048$ for the Kaibab plateau and $L = 8\,192$ for the Wasatch front data sets.

Dataset	MPR			SV-MPR (BST)			SV-MPR (SST)		
	MAAE	MRASE	t[s]	MAAE	MRASE	t[s]	MAAE	MRASE	t[s]
Kaibab plateau	5.00	7.05	0.175	4.81	6.53	0.161	4.98	6.68	0.193
Wasatch front	26.14	35.60	2.64	23.36	32.58	2.44	24.22	33.37	3.02

the **MPR** method. Indeed, the **SV-MPR** implementations reduce the **MPR** MAAE errors by 4-11% (BST) and 0.4-7.4% (SST) and the MRASE errors by 7.4-8.5% (BST) and 5.3-6.3% (SST).

As for the computational efficiency, some comments are in order. Compared to the original **MPR** approach, one can notice overall only a small reduction of t (if any) achieved by the BST

implementation and even some increase by applying the SST implementation. This might appear as contradiction with the above results for Walker lake data, presented in Table 2, but it has a simple explanation. The total execution time largely depends on the speed of the convergence to equilibrium, as the rest is only dictated by the number of samples needed for averaging and is almost independent of the chosen method. However, as explained above and demonstrated in Fig. 10, the SV-MPR implementations are indeed either faster in reaching the equilibrium state (BST) or more efficient in finding states with the energy levels lower than those achievable by the MPR method (SST). The reason why the shorter BST equilibration time is not more apparently reflected in the values of t is that, for simplicity, in all the methods we used the same (default) values of the parameter $n_{fit} = 20$, which defines the memory length of the energy time series employed in testing the onset of equilibrium, and the parameter $n_f = 5$, which defines the frequency of verification of equilibrium conditions². Thus, in all the used approaches the first checking of the equilibrium conditions is only performed after the first $n_{fit} + n_f = 25$ MC sweeps, regardless of the fact that in some cases the equilibrium is reached much faster. For example, from Fig. 10 we can see that the equilibrium conditions of the BST implementation are already reached at about 20 MC sweeps even for as big data as Wasatch front. On the other hand, the SST implementation requires more (about 25) MC sweeps but it reaches lower energy levels. Additional contribution, which further increases the total SST execution time, comes from the temperature smoothing procedure. Thus, the execution time of the SV-MPR implementations can be in principle shortened by resetting of the concerned parameters. However, considering the superior efficiency of all the MPR-based methods compared to some other approaches (e.g., see comparison with IDW in Fig. 14), at present we find it unessential.

3.5 Effect of SV-MPR parameters

In the above study we used the SV-MPR methods with the fixed block size $l_b = 32$ and in the SST implementation the fixed smoothing parameter $n_s = 5$. In the following we demonstrate the effect of these parameters on the prediction performance of the respective methods. The latter is demonstrated in Fig. 12, in which the prediction errors of the SV-MPR method, err_{SV-MPR} , are presented relative to those obtained from the simple MPR method, err_{MPR} for two cases of a relatively small ($p = 0.3$) and large ($p = 0.8$) degrees of thinning. In Fig. 12(a) they are shown for the BST implementation considering different block sizes l_b and in Fig. 12(b) for the SST implementation with the fixed $l_b = 32$ and a varying parameter n_s . As one can see from Fig. 12(a), the above used block size $l_b = 32$ may not be optimal in terms of minimizing prediction errors. As discussed in the previous section, its decreasing allows a greater flexibility in capturing the local variability, which may result in improvement of the prediction performance. On the other hand, smaller values of l_b in combination with larger values of p suffer from the lack of the sampling points within the blocks, which may lead to the block-specific parameters misestimation and consequently deterioration of the prediction accuracy.

Figure 12(b) shows that the smoothing parameter n_s not only suppresses the edge-like visual artifacts but its choice can also affect the prediction performance of the SST implementation. In particular, the gradual smoothing tends to increase MAAE and decrease (to smaller extent) MRASE and its effect is more pronounced in data with larger sparsity. Therefore, relatively small

² For detailed description of n_{fit} and n_f see also paper by Žukovič et al. (2020).

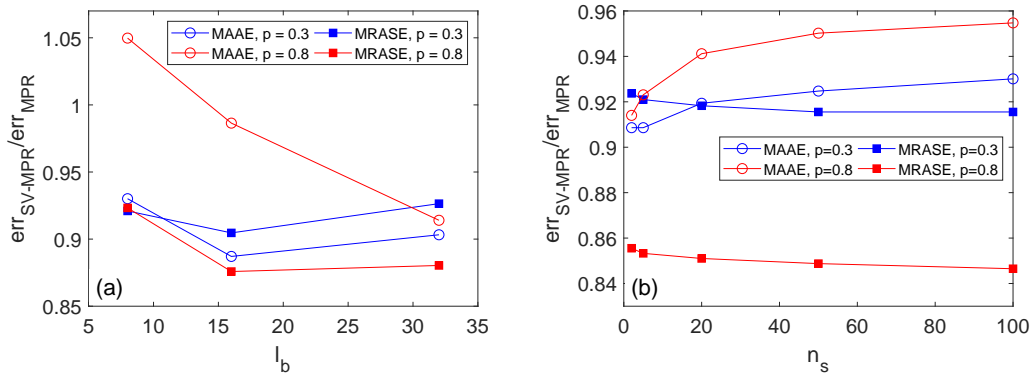


Fig. 12 (a) Errors of the **SV-MPR** method, err_{SV-MPR} , relative to those obtained from the simple **MPR** method, err_{MPR} , as functions of (a) the block size l_b in the BST implementation and (b) the smoothing parameter n_s in the SST implementation.

values of the smoothing parameter, such as $n_s \approx 5$, which to some degree suppress the visual artifacts but still do not excessively increase MAAE, may be considered as an acceptable compromise. In any case, compared to the standard **MPR** method, the SST implementation of the **SV-MPR** method appears to deliver superior prediction performance for arbitrary choice of the parameter n_s .

3.6 Comparison with established IDW approach

Prediction performance and computational efficiency of the original **MPR** method have been compared with several established interpolation methods (Žukovič and Hristopoulos, 2018). Among them, the inverse distance weighted (IDW) (Shepard, 1968) and the ordinary kriging (OK) Wackernagel (2003) were the methods that gave the prediction performance comparable with the **MPR** approach. However, the high computational complexity of OK prevents it to be applied to huge data sets. Therefore, for comparison of the present GPU-implemented **MPR**-based methods we chose the GPU-implemented IDW method (Marcellino et al., 2017) by using the CUDA code available at GitHub (Ruggieri and Marcellino, 2017). The implementation of IDW involves choosing two parameters, which can influence both the prediction performance and computational efficiency. The power parameter was set to a default value of 2 and the search radius R was varied from the minimum for which every prediction point has some sample points within the radius up to the maximum involving practically all points on the grid. We note that an optimal choice of R is not so obvious. It can be set to some fixed value equal for all points, which can result in the problem of some prediction points not having any samples in the search radius, or it can be made variable, which would make the IDW implementation more involved. In particular, in Fig. 13 we present errors of the **MPR** (blue color) and **SV-MPR** BST (red color) methods, relative to those obtained from the IDW method, err_{MPR}/err_{IDW} and err_{BST}/err_{IDW} , as functions of the search radius R , for (a) Walker lake and (b) Wasatch front data sets. Therefore, the values larger than 1 mean superior performance of IDW. One can notice that IDW shows the best prediction performance for the smallest search radius R , where it outperforms both **MPR** as well as **SV-MPR** BST methods.

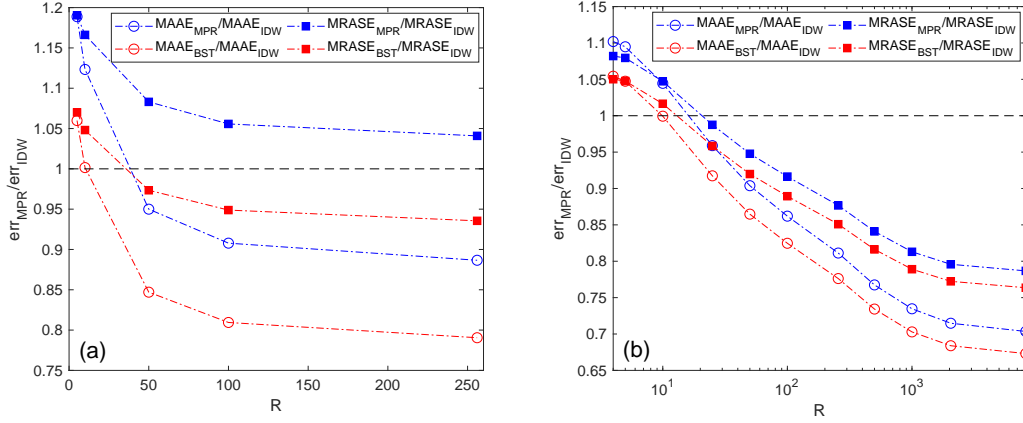


Fig. 13 MAAE (open circles) and MRASE (filled squares) errors of the **MPR** (blue color) and **SV-MPR** BST (red color) methods, relative to those obtained from the IDW method, as functions of the search radius R , for (a) Walker lake and (b) Wasatch front data sets.

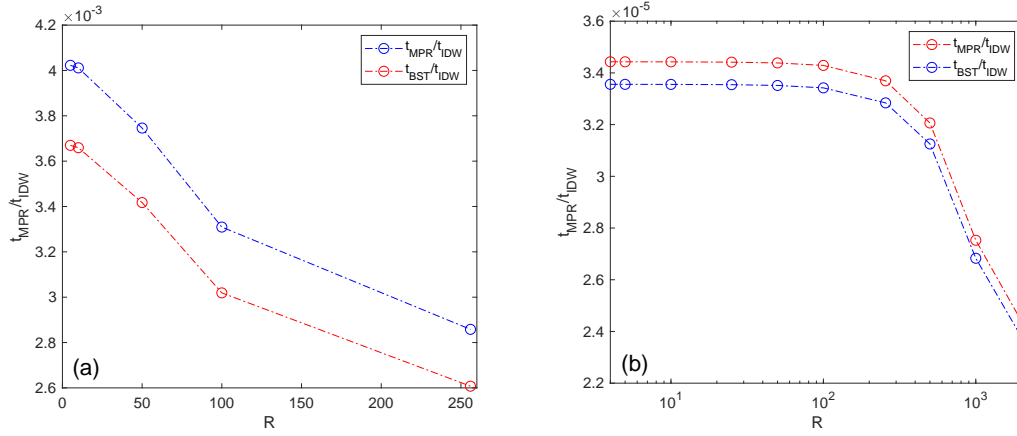


Fig. 14 GPU time of the **MPR** (blue color) and **SV-MPR** BST (red color) methods, relative to those required by the IDW method, as functions of the IDW search radius R , for (a) the Walker lake and (b) Kaibab plateau data sets.

However, with the increasing R the IDW errors increase and in most cases (except MAAE error for Walker Lake data) starting from some value of R both **MPR**-based methods become superior. Owing to the improved prediction performance of the present **SV-MPR** BST implementation, the latter outperforms IDW starting from much smaller R than the standard **MPR** method. Even for the optimal IDW performance at small R , the errors of the **SV-MPR** BST method do not exceed those from IDW by more than 5 – 7% .

On the other hand, the computational efficiency of the **MPR**-based methods clearly dominates over the IDW performance, regardless of the parameters. Due to favorable scaling properties of the **MPR** method (computational time scales approximately linearly with system size) its dominance

over IDW further increases with the data size. As presented in Fig. 14, the ratio of the GPU execution times of the **MPR**-based to IDW methods is of the order of 10^{-3} for relatively small Walker lake data set ($L = 256$) and of the order of 10^{-5} for much larger Kaibab plateau data set ($L = 2\,048$). We note that for as massive data as Wasatch front ($L = 8\,192$) the IDW calculations could not be executed on a standard GPU-equipped PC within some reasonable time at all³. The curves presented in Fig. 14 also show that the relative computational efficiency of the **MPR**-based methods, as expected, increases with the search radius R due to decreasing efficiency of IDW. Furthermore, by comparing the results for the two **MPR** based approaches one can see that the **SV-MPR** BST method is somewhat faster than the original **MPR** approach, again in line with the expectations discussed above.

4 Conclusions

In the current study we proposed a rather general approach to modelling spatial heterogeneity, the feature often present in massive spatial data, in GPU-implemented spatial prediction methods for gridded data. In particular, we presented two approaches to introducing spatial dependence to the model parameter (temperature) by the so-called double-checkerboard (DC) decomposition to our previously introduced GPU-accelerated **MPR** method and thus obtained two **SV-MPR** methods with spatially varying temperatures. In the BST variation, separate values of the temperature are obtained for each block of the DC-decomposed grid and in the SST variation even each individual prediction point is modelled using its own temperature. Then, similar to the **MPR** method, predictions of unknown values are obtained from conditional situations. However, in the present methods the conditional situations are actually non-equilibrium but assume “local” equilibrium conditions corresponding to the local temperatures. Using various types of big heterogeneous real data, such as remote sensing data, we have demonstrated that the proposed **SV-MPR** methods significantly improve prediction performance and even computational efficiency of the original **MPR** method. Their prediction performance is competitive with some established prediction methods, such as IDW, but their execution times are by several orders of magnitude faster. We note that the presented approach to modelling spatial heterogeneity was demonstrated on the **MPR** method but in fact it is rather general and its application to other GPU-implemented methods is rather straightforward.

Future extensions of the presented models to further increase their flexibility and ability to capture various relevant features present in real data, such as geometric anisotropy or non-Gaussianity, may involve adding more parameters to the temperature, while still keeping their local nature (within blocks) and spatial variability. For example, the geometric anisotropy could be introduced by distinguishing the exchange interactions in different directions, i.e., by introducing a directional exchange interaction anisotropy parameter. The non-Gaussianity could be incorporated by including higher-order interactions and/or applying some suitable form of an external “magnetic” (bias) field to the Hamiltonian. Another possibility to be considered is inclusion of further-neighbor pairwise interactions that would, for example, control data smoothness. The impressive computational efficiency of the models offers possibility to extend them to three dimensions (3D space or 2D space + time), where there is still lack of efficient methods that would enable modeling massive data (Wang et al., 2012). The generalization of the GPU code from two to three dimensions is

³ We terminated the calculation after about two weeks of running and the errors presented in Fig. 13(b) were obtained by executing the code on the supercomputer Govorun at the Joint Institute for Nuclear Research in Dubna.

straightforward. The GPU time in 3D is expected to increase by the factor of 3/2 but the relative efficiency of the CPU and GPU implementations should be preserved (Weigel, 2012).

CRedit authorship contribution statement

Matúš Lach: Software, Investigation, Data curation, Visualization, Validation, Writing – original draft preparation. **Milan Žukovič:** Conceptualization, Methodology, Formal analysis, Validation, Writing – review and editing, Supervision. All authors contributed to the writing of the manuscript.

Declaration of competing interest

The authors declare that they have no known competing financial interests or personal relationships that could have appeared to influence the work reported in this paper.

Acknowledgements

This work was supported by the Scientific Grant Agency of Ministry of Education of Slovak Republic (Grant No. 1/0531/19) and the Slovak Research and Development Agency (Grant No. APVV-20-0150).

Computer code availability

Name of the code/library: packages MPR, SV – MPR (BST), and SV – MPR (SST)
Contact: e-mail and phone number: matus.lach@gmail.com, +421 915 609 735
Hardware requirements: NVIDIA GPU with compute capability 5.2 or higher (GTX 950 or newer)
Program language: CUDA
Software required: CUDA 10.1, CUB library, Windows or Linux operating system (not tested on OS X)
Program size in zipped format: 5 MB for MPR, 3.3 MB for SV – MPR (BST), and 9.4 MB for
The source codes are available for downloading at the links: <https://github.com/MatusLach/MPR>;
https://github.com/MatusLach/SV-MPR_BST; https://github.com/MatusLach/SV-MPR_SST

References

- Bai, T., Tahmasebi, P., 2021. Accelerating geostatistical modeling using geostatistics-informed machine learning. *Computers & Geosciences* 146, 104663.
- Bechle, M.J., Millet, D.B., Marshall, J.D., 2013. Remote sensing of exposure to no2: Satellite versus ground-based measurement in a large urban area. *Atmospheric Environment* 69, 345–353.
- Cheng, T., 2013. Accelerating universal kriging interpolation algorithm using CUDA-enabled GPU. *Computers & Geosciences* 54, 178 – 183. doi:<https://doi.org/10.1016/j.cageo.2012.11.013>.

- Cheng, T., Li, D., Wang, Q., 2010. On parallelizing universal kriging interpolation based on OpenMP, in: 2010 Ninth International Symposium on Distributed Computing and Applications to Business, Engineering and Science, pp. 36–39.
- Coleman, J.B., Yao, X., Jordan, T.R., Madden, M., 2011. Holes in the ocean: Filling voids in bathymetric lidar data. *Computers & geosciences* 37, 474–484.
- Cressie, N., Johannesson, G., 2018. Fixed rank kriging for very large spatial data sets. *Journal of the Royal Statistical Society: Series B (Statistical Methodology)* 70, 209–226. URL: <https://rss.onlinelibrary.wiley.com/doi/abs/10.1111/j.1467-9868.2007.00633.x>, doi:10.1111/j.1467-9868.2007.00633.x, arXiv:<https://rss.onlinelibrary.wiley.com/doi/pdf/10.1111/j.1467-9868.2007.00633.x>
- Emmendorfer, L.R., Dimuro, G.P., 2021. A point interpolation algorithm resulting from weighted linear regression. *Journal of Computational Science* 50, 101304. URL: <https://www.sciencedirect.com/science/article/pii/S1877750321000053>, doi:<https://doi.org/10.1016/j.jocs.2021.101304>.
- Finley, A.O., 2011. Comparing spatially-varying coefficients models for analysis of ecological data with non-stationary and anisotropic residual dependence. *Methods in Ecology and Evolution* 2, 143–154.
- Fotheringham, A.S., Brunson, C., Charlton, M., 2003. Geographically weighted regression: the analysis of spatially varying relationships. John Wiley & Sons.
- Furrer, R., Genton, M.G., Nychka, D., 2006. Covariance tapering for interpolation of large spatial datasets. *Journal of Computational and Graphical Statistics* 15, 502–523. URL: <https://doi.org/10.1198/106186006X132178>, doi:10.1198/106186006X132178, arXiv:<https://doi.org/10.1198/106186006X132178>.
- Gelfand, A.E., Kim, H.J., Sirmans, C., Banerjee, S., 2003. Spatial modeling with spatially varying coefficient processes. *Journal of the American Statistical Association* 98, 387–396.
- Guan, Q., Kyriakidis, P.C., Goodchild, M.F., 2011. A parallel computing approach to fast geostatistical areal interpolation. *International Journal of Geographical Information Science* 25, 1241–1267. doi:10.1080/13658816.2011.563744.
- Harris, M., 2007. Optimizing Parallel Reductions in CUDA. URL: <https://developer.download.nvidia.com/assets/cuda/files/reduction.pdf>. <https://developer.download.nvidia.com/assets/cuda/files/reduction.pdf>.
- Harris, P., Fotheringham, A., Crespo, R., Charlton, M., 2010a. The use of geographically weighted regression for spatial prediction: an evaluation of models using simulated data sets. *Mathematical Geosciences* 42, 657–680.
- Harris, R., Singleton, A., Grose, D., Brunson, C., Longley, P., 2010b. Grid-enabling geographically weighted regression: a case study of participation in higher education in England. *Transactions in GIS* 14, 43–61.
- Hartman, L., Hössjer, O., 2008. Fast kriging of large data sets with Gaussian Markov random fields. *Computational Statistics & Data Analysis* 52, 2331 – 2349. URL: <http://www.sciencedirect.com/science/article/pii/S0167947307003568>, doi:<https://doi.org/10.1016/j.csda.2007.09.018>.
- Hristopulos, D., 2003. Spartan Gibbs random field models for geostatistical applications. *SIAM Journal on Scientific Computing* 24, 2125–2162. doi:10.1137/S106482750240265X.
- Hristopulos, D.T., 2015. Stochastic local interaction (sli) model. *Computers & Geosciences* 85, 26–37. doi:10.1016/j.cageo.2015.05.018.
- Hristopulos, D.T., Elogne, S.N., 2007. Analytic properties and covariance functions for a new class of generalized Gibbs random fields. *IEEE Transactions on Information Theory* 53, 4667–4679.

- doi:[10.1109/TIT.2007.909163](https://doi.org/10.1109/TIT.2007.909163).
- Hristopulos, D.T., Pavlides, A., Agou, V.D., Gkafa, P., 2021. Stochastic local interaction model: An alternative to kriging for massive datasets. *Mathematical Geosciences* 53, 1907–1949.
- Hu, H., Shu, H., 2015. An improved coarse-grained parallel algorithm for computational acceleration of ordinary kriging interpolation. *Computers & Geosciences* 78, 44 – 52. URL: <http://www.sciencedirect.com/science/article/pii/S0098300415000333>, doi:<https://doi.org/10.1016/j.cageo.2015.02.011>.
- Ingram, B., Cornford, D., Evans, D., 2008. Fast algorithms for automatic mapping with space-limited covariance functions. *Stochastic Environmental Research and Risk Assessment* 22, 661–670. URL: <https://doi.org/10.1007/s00477-007-0163-9>, doi:[10.1007/s00477-007-0163-9](https://doi.org/10.1007/s00477-007-0163-9).
- Isaaks, E., Srivastava, R., 1989. *Applied geostatistics*. Oxford University Press, New York.
- Kadlec, J., Ames, D.P., 2017. Using crowdsourced and weather station data to fill cloud gaps in modis snow cover datasets. *Environmental Modelling & Software* 95, 258–270.
- Kaufman, C.G., Schervish, M.J., Nychka, D.W., 2008. Covariance tapering for likelihood-based estimation in large spatial data sets. *Journal of the American Statistical Association* 103, 1545–1555. URL: <https://doi.org/10.1198/01621450800000959>, doi:[10.1198/01621450800000959](https://doi.org/10.1198/01621450800000959), [arXiv:https://doi.org/10.1198/01621450800000959](https://arxiv.org/abs/https://doi.org/10.1198/01621450800000959).
- Kerry, K.E., Hawick, K.A., 1998. Kriging interpolation on high-performance computers, in: Sloat, P., Bubak, M., Hertzberger, B. (Eds.), *High-Performance Computing and Networking*, Springer Berlin Heidelberg, Berlin, Heidelberg. pp. 429–438.
- Lajaunie, C., Renard, D., Quentin, A., Le Guen, V., Caffari, Y., 2020. A non-homogeneous model for kriging dosimetric data. *Mathematical Geosciences* 52, 847–863.
- Lehman, J., Swinton, K., Bortnick, S., Hamilton, C., Baldrige, E., Eder, B., Cox, B., 2004. Spatio-temporal characterization of tropospheric ozone across the eastern united states. *Atmospheric Environment* 38, 4357–4369.
- Li, Z., Fotheringham, A.S., Li, W., Oshan, T., 2019. Fast geographically weighted regression (fast-gwr): a scalable algorithm to investigate spatial process heterogeneity in millions of observations. *International Journal of Geographical Information Science* 33, 155–175.
- Luitjens, J., 2014. Faster Parallel Reductions on Kepler. URL: <https://devblogs.nvidia.com/faster-parallel-reductions-kepler/>.
<https://devblogs.nvidia.com/faster-parallel-reductions-kepler/>.
- MacGillivray, M., Hunter, D., Jan, N., 1993. “local” equilibrium monte carlo simulations. *Physica A: Statistical Mechanics and its Applications* 197, 144–152.
- Marcellino, L., Montella, R., Kosta, S., Galletti, A., Di Luccio, D., Santopietro, V., Ruggieri, M., Lapegna, M., D’Amore, L., Laccetti, G., 2017. Using gpgpu accelerated interpolation algorithms for marine bathymetry processing with on-premises and cloud based computational resources, in: *International Conference on Parallel Processing and Applied Mathematics*, Springer. pp. 14–24.
- Marcotte, D., Allard, D., 2018. Half-tapering strategy for conditional simulation with large datasets. *Stochastic Environmental Research and Risk Assessment* 32, 279–294. URL: <https://doi.org/10.1007/s00477-017-1386-z>, doi:[10.1007/s00477-017-1386-z](https://doi.org/10.1007/s00477-017-1386-z).
- Mariethoz, G., 2010. A general parallelization strategy for random path based geostatistical simulation methods. *Computers & Geosciences* 36, 953–958.
- Mei, G., 2014. Evaluating the power of GPU acceleration for IDW interpolation algorithm. *The Scientific World Journal* 2014, 1715741 – 8. doi:<http://dx.doi.org/10.1155/2014/171574>.

- Mei, G., Xu, L., Xu, N., 2017. Accelerating adaptive inverse distance weighting interpolation algorithm on a graphics processing unit. *Open Science* 4, 170436. URL: <http://rsos.royalsocietypublishing.org/content/4/9/170436>, doi:[10.1098/rsos.170436](https://doi.org/10.1098/rsos.170436), arXiv:<http://rsos.royalsocietypublishing.org/content/4/9/170436.full.pdf>.
- Migallón, V., Navarro-González, F.J., Penadés, H., Penadés, J., Villacampa, Y., 2022. A parallel methodology using radial basis functions versus machine learning approaches applied to environmental modelling. *Journal of Computational Science* 63, 101817. URL: <https://www.sciencedirect.com/science/article/pii/S1877750322001831>, doi:<https://doi.org/10.1016/j.jocs.2022.101817>.
- Misra, C., Bhattacharya, S., Ghosh, S.K., 2020. A fast scalable distributed kriging algorithm using spark framework. *International Journal of Data Science and Analytics* 10, 249–264.
- Murakami, D., Tsutsumida, N., Yoshida, T., Nakaya, T., Lu, B., 2020. Scalable gwr: A linear-time algorithm for large-scale geographically weighted regression with polynomial kernels. *Annals of the American Association of Geographers* 111, 459–480.
- Nunes, R., Almeida, J.A., 2010. Parallelization of sequential gaussian, indicator and direct simulation algorithms. *Computers & Geosciences* 36, 1042–1052.
- Nvidia, 2021. *CUDA C++ Programming Guide*. URL: <http://docs.nvidia.com/cuda/cuda-c-programming-guide/index.html>.
<http://docs.nvidia.com/cuda/cuda-c-programming-guide/index.html>.
- Oyebamiji, O., Wilkinson, D., Jayathilake, P., Curtis, T., Rushton, S., Li, B., Gupta, P., 2017. Gaussian process emulation of an individual-based model simulation of microbial communities. *Journal of Computational Science* 22, 69–84. URL: <https://www.sciencedirect.com/science/article/pii/S1877750317300443>, doi:<https://doi.org/10.1016/j.jocs.2017.08.006>.
- Pardo-Igúzquiza, E., Dowd, P.A., Grimes, D.I., 2005. An automatic moving window approach for mapping meteorological data. *International Journal of Climatology: A Journal of the Royal Meteorological Society* 25, 665–678.
- Peredo, O., Ortiz, J.M., Herrero, J.R., 2015. Acceleration of the geostatistical software library (gslib) by code optimization and hybrid parallel programming. *Computers & Geosciences* 85, 210–233.
- Pesquer, L., Cortés, A., Pons, X., 2011. Parallel ordinary kriging interpolation incorporating automatic variogram fitting. *Computers & Geosciences* 37, 464 – 473. URL: <http://www.sciencedirect.com/science/article/pii/S0098300410003341>, doi:<https://doi.org/10.1016/j.cageo.2010.10.010>.
- Que, X., Ma, C., Ma, X., Chen, Q., 2021. Parallel computing for fast spatiotemporal weighted regression. *Computers & Geosciences* 150, 104723.
- Rasera, L.G., Machado, P.L., Costa, J.F.C., 2015. A conflict-free, path-level parallelization approach for sequential simulation algorithms. *Computers & Geosciences* 80, 49–61.
- de Ravé, E.G., Jiménez-Hornero, F., Ariza-Villaverde, A., Gómez-López, J., 2014. Using general-purpose computing on graphics processing units (GPGPU) to accelerate the ordinary kriging algorithm. *Computers & Geosciences* 64, 1–6. doi:<https://doi.org/10.1016/j.cageo.2013.11.004>.
- Ruggieri, M., Marcellino, L., 2017. Parallel gpu inverse distance weighting. <https://github.com/MarioRuggieri/G-IDW>.
- Shepard, D., 1968. A two-dimensional interpolation function for irregularly-spaced data, in: *Proceedings of the 1968 23rd ACM national conference*, pp. 517–524.

- Sickles, J.E., Shadwick, D.S., 2007. Effects of missing seasonal data on estimates of period means of dry and wet deposition. *Atmospheric Environment* 41, 4931 – 4939. URL: <http://www.sciencedirect.com/science/article/pii/S1352231007001318>, doi:<https://doi.org/10.1016/j.atmosenv.2007.01.052>.
- State of Utah, 2015. State of Utah Acquired LiDAR Data - Wasatch Front. doi:<https://doi.org/10.5069/G9TH8JNQ>. Distributed by OpenTopography. <https://doi.org/10.5069/G9TH8JNQ>.
- Stojanovic, N., Stojanovic, D., 2014. High performance processing and analysis of geospatial data using CUDA on GPU. *Advances in Electrical and Computer Engineering* 14, 109–114. doi:[doi:10.4316/AECE.2014.04017](https://doi.org/10.4316/AECE.2014.04017).
- Sun, L., Chen, Z., Gao, F., Anderson, M., Song, L., Wang, L., Hu, B., Yang, Y., 2017. Reconstructing daily clear-sky land surface temperature for cloudy regions from modis data. *Computers & Geosciences* 105, 10–20.
- Tahmasebi, P., Sahimi, M., Mariethoz, G., Hezarkhani, A., 2012. Accelerating geostatistical simulations using graphics processing units (GPU). *Computers & Geosciences* 46, 51–59. doi:<https://doi.org/10.1016/j.cageo.2012.03.028>.
- Tran, H.T., Nguyen, H.T., Tran, V.T., 2016. Large-scale geographically weighted regression on spark, in: 2016 Eighth International Conference on Knowledge and Systems Engineering (KSE), IEEE. pp. 127–132.
- US Forest Service, 2019. Mapping the Kaibab Plateau, AZ. doi:<https://doi.org/10.5069/G9TX3CH3>. Collected by 3Di West, distributed by OpenTopography. <https://doi.org/10.5069/G9TX3CH3>.
- Žukovič, M., Hristopoulos, D.T., 2018. Gibbs markov random fields with continuous values based on the modified planar rotator model. *Physical Review E* 98, 062135. URL: <https://link.aps.org/doi/10.1103/PhysRevE.98.062135>, doi:[10.1103/PhysRevE.98.062135](https://doi.org/10.1103/PhysRevE.98.062135).
- Wackernagel, H., 2003. *Multivariate Geostatistics*. 3rd ed., Springer-Verlag Berlin Heidelberg.
- Wang, G., Garcia, D., Liu, Y., de Jeu, R., Johannes Dolman, A., 2012. A three-dimensional gap filling method for large geophysical datasets: Application to global satellite soil moisture observations. *Environmental Modelling & Software* 30, 139–142. URL: <https://linkinghub.elsevier.com/retrieve/pii/S1364815211002453>, doi:[10.1016/j.envsoft.2011.10.015](https://doi.org/10.1016/j.envsoft.2011.10.015).
- Weigel, M., 2011. Simulating spin models on GPU. *Computer Physics Communications* 182, 1833 – 1836. URL: <http://www.sciencedirect.com/science/article/pii/S0010465510004327>, doi:<https://doi.org/10.1016/j.cpc.2010.10.031>. computer Physics Communications Special Edition for Conference on Computational Physics Trondheim, Norway, June 23-26, 2010.
- Weigel, M., 2012. Performance potential for simulating spin models on GPU. *Journal of Computational Physics* 231, 3064 – 3082. URL: <http://www.sciencedirect.com/science/article/pii/S0021999111007066>, doi:<https://doi.org/10.1016/j.jcp.2011.12.008>.
- Wiens, A., Nychka, D., Kleibe, W., 2020. Modeling spatial data using local likelihood estimation and a mat\`ern to sar translation. arXiv preprint arXiv:2002.01124 .
- Xia, Y.J., Kuang, L., Li, X.M., 2011. Accelerating geospatial analysis on GPUs using CUDA. *Journal of Zhejiang University, Science C* 12, 990–999. doi:[10.1631/jzus.C1100051](https://doi.org/10.1631/jzus.C1100051).
- Zhang, W., Li, W., Zhang, C., Zhao, T., 2019. Parallel computing solutions for Markov chain spatial sequential simulation of categorical fields. *International Journal of Digital Earth* 12,

- 566–582. doi:[10.1080/17538947.2018.1464073](https://doi.org/10.1080/17538947.2018.1464073).
- Zhang, Y., Zheng, X., Wang, Z., Ai, G., Huang, Q., 2018. Implementation of a parallel gpu-based space-time kriging framework. *ISPRS International Journal of Geo-Information* 7, 193. URL: <http://www.mdpi.com/2220-9964/7/5/193>, doi:[10.3390/ijgi7050193](https://doi.org/10.3390/ijgi7050193).
- Zhong, X., Kealy, A., Duckham, M., 2016. Stream kriging: Incremental and recursive ordinary kriging over spatiotemporal data streams. *Computers & Geosciences* 90, 134 – 143. doi:<https://doi.org/10.1016/j.cageo.2016.03.004>.
- Žukovič, M., Borovský, M., Lach, M., Hristopulos, D.T., 2020. Gpu-accelerated simulation of massive spatial data based on the modified planar rotator model. *Mathematical Geosciences* 52, 123–143.
- Žukovič, M., Hristopulos, D.T., 2009a. Classification of missing values in spatial data using spin models. *Physical Review E* 80, 011116. URL: <https://link.aps.org/doi/10.1103/PhysRevE.80.011116>, doi:[10.1103/PhysRevE.80.011116](https://doi.org/10.1103/PhysRevE.80.011116).
- Žukovič, M., Hristopulos, D.T., 2009b. Multilevel discretized random field models with 'spin' correlations for the simulation of environmental spatial data. *Journal of Statistical Mechanics: Theory and Experiment* 2009, P02023.